

Banner appropriate to article type will appear here in typeset article

# Bulldozing an immersed granular material in a confined channel

Liam C. Morrow<sup>1†</sup>, Oliver W. Paulin<sup>1</sup>, Matthew G. Hennessy<sup>2</sup>, Duncan R. Hewitt<sup>3</sup>, Miles L. Morgan<sup>4</sup>, Bjørnar Sandnes<sup>4</sup>, and Christopher W. MacMinn<sup>1</sup>

<sup>1</sup>Department of Engineering Science, University of Oxford, Oxford OX1 3PJ, United Kingdom

<sup>2</sup>School of Engineering Mathematics and Technology, University of Bristol, Bristol, BS8 1TW, United Kingdom

<sup>3</sup>Department of Applied Mathematics and Theoretical Physics, University of Cambridge, Cambridge, CB3 0WA, United Kingdom

<sup>4</sup>Department of Chemical Engineering, Swansea University, Swansea, SA1 8EN, United Kingdom

(Received xx; revised xx; accepted xx)

The motion of an immersed granular material in a channel is characterised by complex interactions among the grains, between the grains and the permeating liquid, and between the grains and the channel walls. Here, we develop a reduced-order continuum model for the bulldozing of an immersed, sedimented granular material by a piston in a channel. In our continuum approach, the granular pile and the overlying fluid layer evolve as a system of coupled thin films. We model the granular phase as a dense, porous, visco-plastic material that experiences Coulomb-like friction with the walls. Conservation of mass and momentum under a thin-film approximation leads to an elliptic equation for the velocity of the grains that is coupled with an evolution equation for the height of the granular pile. We solve our model numerically for a variety of different scenarios to explore the interactions between wall friction, internal viscous-like stresses, and fluid flow above and through the pile. We complement our numerical results with a series of experiments that provide insight into the validity and limitations of the model.

## 1. Introduction

Depending on the confining stress, granular media can respond mechanically at the continuum scale as a solid, liquid, or gas (Forterre & Pouliquen 2008). Granular flows are relevant to a wide variety of natural processes, including avalanches (Doppler *et al.* 2007; Pailha & Pouliquen 2009), terrestrial and submarine landslides (Hampton *et al.* 1996; Legros 2002), blood flows through small vessels (Freund & Orescanin 2011), and debris flows (Iverson 1997), as well as to a variety of industrial applications. The continuum rheology of granular media has been studied extensively, primarily focusing on internal friction and thus on relative motion and sliding *within* the granular material. For example, many studies consider scenarios in which a granular material is confined and sheared between a fixed plate or cylinder and a moving one (Aussillous *et al.* 2013; Houssais *et al.* 2016; Maurin *et al.* 2016; Ouriemi *et al.* 2009), whereas classical bedload transport involves the shearing of an unconfined granular

† Email address for correspondence: liam.morrow@eng.ox.ac.uk

material by an overlying fluid flow (Frey & Church 2011). Avalanche-type flows have also attracted substantial attention, in which an unconfined granular material flows downhill under gravity (Bouchut *et al.* 2016; Cassar *et al.* 2005; Doppler *et al.* 2007; Forterre & Pouliquen 2008; Pailha & Pouliquen 2009). Finally, Sauret *et al.* (2014) studied the unconfined pile-up of a granular material during bulldozing by a vertical plate on a rotating table, focusing on the initial growth of the pile and then on its long-time shape.

Additional challenges arise in confined granular-flow problems where the grains are able to slide along the confining walls. The flow of sand through an hourglass is a relatable example; similar interactions occur within subsurface faults and fractures (Dorostkar *et al.* 2017) and in silos (Janssen 1895; Landry *et al.* 2003). This class of problems has received less attention. Some authors have considered the impact of the confining vertical side walls on avalanche-type flows in channels (Jop *et al.* 2005; Taberlet *et al.* 2008; Artoni & Richard 2015). Simulations and experiments show that these walls can have a significant impact on the flow, potentially changing the convexity of the flow profile if the channel is sufficiently narrow. Marks *et al.* (2015) used the discrete-element method (DEM) to simulate the piston-driven bulldozing of dry grains between horizontal top and bottom plates in two spatial dimensions. It was found that, as the pile grows and then bridges the gap between the two plates, the bulldozing force grows exponentially with the length of the bridged region due to sliding friction between the grains and the plates, which is consistent with the classical Janssen effect (Janssen 1895). Morgan *et al.* (2020) performed experiments to study the fluid-driven motion of granular material along a confined, quasi-2D channel.

Additional inspiration for the present study comes from a series of experiments involving the bulldozing of grains by capillary forces. This problem has been considered in both one- and two-dimensional geometries. In the one-dimensional case, air was injected into a capillary tube containing a wet granular suspension (Dumazer *et al.* 2016; Dumazer, G. and Sandnes, B. and Måløy, K. J. and Flekkøy 2020). As the air is non-wetting to the grains, the liquid-gas meniscus acts to bulldoze the grains like a piston. When the gap is bridged and the granular plug becomes jammed, the gas phase percolates through the static plug and emerges out the other side, resulting in a repeating pattern of granular plugs dispersed between gas regions. In the two-dimensional case of a Hele-Shaw cell, the system has more degrees of freedom (Eriksen *et al.* 2018; Sandnes *et al.* 2007, 2011; Zhang *et al.* 2023). In this case, at the point of jamming, the gas pushes in the direction of least resistance, resulting in the creation of a fingering pattern whose morphology is distinct from traditional viscous fingers that form in the absence of the solid phase (Paterson 1981; Saffman & Taylor 1958). Ad hoc, rule-based simulations can do an excellent job of reproducing these patterns (Eriksen *et al.* 2015*b,a*; Knudsen *et al.* 2008), but a true quasi-1D or quasi-2D continuum model derived from the fundamental mechanics of the problem is still lacking.

Despite these previous studies, the nature of the relationship between the motion of grains and their confining geometry remains somewhat elusive, particularly in the case where the grains are being bulldozed. We focus here on determining how the geometry influences the velocity profile of the grains and the resulting shape of the granular pile. To do so, we propose a continuum model to describe the bulldozing of an immersed granular material in a confined geometry. The problem we consider, illustrated in Figure 1, involves two parallel plates separated by a small gap. The gap is filled with a combination of spherical grains (“beads”) and a fluid, and the beads settle out of suspension and form a uniform pile on the bottom plate. From one end of the geometry, a piston moves left to right at a constant velocity and bulldozes the grains. The height of the granular pile grows until the grains bridge the gap between the plates, at which point the grains experience friction with both the bottom and top plates, and as the length of this bridged region grows, the force required to push the piston increases. This problem is a generalisation of the work by Marks *et al.*

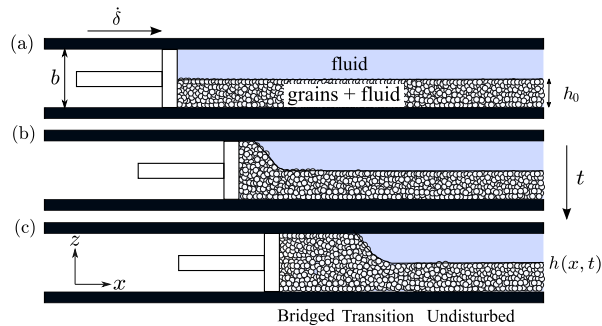


Figure 1: A schematic of granular bulldozing in a confined, horizontal channel. (a) The system consists of two parallel plates separated by a gap  $b$ . The gap is initially filled with a mixture of fluid and beads, where the beads initially occupy a uniform, fluid saturated layer of height  $h_0$  on the bottom plate. (b) A piston moves from left to right with velocity  $\delta$  bulldozing both grains and fluid. As the beads pile up, they will eventually bridge the gap between the plates. (c) As bulldozing continues, the domain comprises three regions: the bridged region where  $h = b$ , the undisturbed region where  $h = h_0$  and the solid is stationary, and the wedged shaped transition region where  $h_0 < h < b$ .

(2015), who considered the limiting case where the fluid phase is ignored. We formulate a two-phase (fluid and solid) two-layer model comprising of a single Newtonian fluid in the top layer and an immersed, dense, porous, granular suspension in the bottom layer, resulting in a depth-averaged system of coupled thin films. Regarding the granular phase, we adopt the so-called  $\mu(I)$  rheology (Jop *et al.* 2005; Pouliquen *et al.* 2006) where  $\mu$  is a rate-dependent effective friction coefficient, which results in the suspension behaving like a pressure-dependent yield-stress fluid. We consider the dimensionless inertial number  $I$  both in the inertial (Midi 2004; Da Cruz *et al.* 2005; Jop *et al.* 2005) and viscous regimes (Cassar *et al.* 2005). The former is generally used when the Stokes number is sufficiently large while the latter is used when an interstitial fluid is present, though effort has been made to combine the two regimes (Baumgarten & Kamrin 2019; Boyer *et al.* 2011; Rettinger *et al.* 2022). Further, we impose a simple Coulomb-like friction model at each of the walls such that the shear stress must be sufficiently large for the beads to slide over the plates Pennestrì *et al.* (2016).

The remainder of this work is organised as follows. In §2, we derive our model based on the approach described above. As previously mentioned, the interactions between the beads and the walls are governed by Coulomb friction. This model gives an expression for the shear stress at the walls only if the beads are in contact with the walls and the magnitude of the shear stress is sufficiently large, which is not known *a priori*. To address this difficulty, we introduce a novel regularisation that gives an expression for the shear stress over the entire computational domain. In §3 and 4, we present a numerical study of our model. In §3 we consider the ‘dry’ limit where the effects of the fluid phase are taken to be negligible. We investigate the velocity profile of the beads both in the regions where the beads have bridged the gap as well as the wedge-shaped transition region illustrated in Fig. 1. In §4 and §5, we focus on the influence of the fluid on the grains, and compare results from our model with laboratory experiments. Finally, in §6, we summarise our findings on the validity of our model and make suggestions for future work.

## 2. Model development

We consider the piston-driven bulldozing of a dense, fluid-saturated granular material in a confined horizontal channel. The channel has a gap of width  $b$  between two parallel, horizontal plates. The gap is filled with an incompressible Newtonian fluid and a granular material with mean grain diameter  $d$ . The solid grains are negatively buoyant and form a uniform layer on the bottom plate of height  $h(x, t)$ , illustrated in Figure 1(a). The granular layer has a uniform initial height  $h_0$ . A rigid piston located at  $x = \delta(t)$  travels from left to right at a constant velocity  $\dot{\delta}$ , bulldozing the grains and the fluid [Figure 1(b) and (c)], where flow in the  $y$ -direction is ignored. We denote the volume fractions of the fluid and solid phases as  $\phi_f$  and  $\phi_s$ , such that  $\phi_f + \phi_s = 1$ . For simplicity, we take  $\phi_s$  to be uniform and equal to a constant  $\phi_s^*$  within the granular layer and zero outside the granular layer. Thus, we neglect elastic compression of the packing and shear-induced dilation of the packing in order to focus on the physical interactions of internal friction, pile-up, wall friction, and fluid flow. The solid fraction  $\phi_s$  is then given by

$$\phi_s(x, z, t) = \begin{cases} \phi_s^*, & \text{for } 0 \leq z \leq h \\ 0, & \text{for } h < z \leq b \end{cases}. \quad (2.1)$$

Defining  $\mathbf{v}_f = u_f(x, z, t)\mathbf{e}_x + w_f(x, z, t)\mathbf{e}_z$  and  $\mathbf{v}_s = u_s(x, z, t)\mathbf{e}_x + w_s(x, z, t)\mathbf{e}_z$  as the velocity of the fluid and solid phases, respectively, then the volume-averaged velocity is  $\mathbf{v} = u(x, z, t)\mathbf{e}_x + w(x, z, t)\mathbf{e}_z = \phi_f\mathbf{v}_f + \phi_s\mathbf{v}_s$ . Conservation of mass for the granular material can then be written in vertically integrated form as

$$\frac{\partial h}{\partial t} + \frac{\partial}{\partial x}(\bar{u}_s h) = 0, \quad (2.2)$$

where

$$\bar{u}_s = \frac{1}{h} \int_0^h u_s \, dz, \quad (2.3)$$

is the average horizontal velocity of the solid. Similarly, by mass conservation, the average horizontal velocity of any vertical slice must be equal to the piston speed,

$$\frac{1}{b} \int_0^b u \, dz = \dot{\delta}. \quad (2.4)$$

### 2.1. Mechanics

We are interested in the parameter space where the Reynolds number  $\text{Re} = \rho_f \dot{\delta} b / \eta_f$  is sufficiently small such that the effects of inertia can be neglected, where  $A$  is the cross-sectional area of the geometry. As such, we have conservation of linear momentum

$$\nabla \cdot \boldsymbol{\sigma} = \rho g \mathbf{e}_z, \quad (2.5)$$

where  $\boldsymbol{\sigma}$  is the total stress in the fluid-solid mixture and  $\rho = \phi_f \rho_f + \rho_s \phi_s$  is the local volume-averaged density of the mixture. Further, we assume that the ratio of horizontal to vertical length scales is sufficiently small such that we impose a lubrication-type approximation where  $w \ll u$  and  $\partial_x \ll \partial_z$ . We discuss the validity of these assumptions in §5.

#### 2.1.1. Upper layer (fluid)

The upper layer comprises of a single incompressible Newtonian fluid of viscosity  $\eta_f$ , for which the lubrication approximation suggests that the fluid pressure  $p_f$  is hydrostatic,

$$p_f(x, z, t) = P_f(x, t) + \rho_f g(b - z),$$

$$\frac{\partial \sigma_{xz}}{\partial z} = \frac{\partial P_f}{\partial x} \quad \text{with} \quad \sigma_{xz} = \eta_f \frac{\partial u_f}{\partial z}, \quad (2.6)$$

where  $P_f$  is the unknown fluid pressure at  $z = b$ . By imposing no-slip boundary conditions  $u_f = 0$  on  $z = b$  and  $u_f = u_s$  on  $z = h$ , we arrive at an expression for the velocity of the fluid in the upper layer

$$u_f(x, z, t) = \frac{(b - z)(h - z)}{2\eta_f} \frac{\partial P_f}{\partial x} + \frac{b - z}{b - h} u_s(z = h), \quad (2.7)$$

while the shear stress exerted on the granular layer by the fluid above is

$$\sigma_{xz}(z = h) = \eta_f \left( \frac{h - b}{2\eta_f} \frac{\partial P_f}{\partial x} - \frac{u_s(z = h)}{b - h} \right). \quad (2.8)$$

Equation (2.7) models the velocity of the fluid in the upper layer via a parabolic Poiseuille shape that is skewed by the potential motion of the granular layer.

### 2.1.2. Lower layer (fluid-solid mixture)

For the bottom layer, we adopt Terzaghi's principal (Terzaghi 1936) such that the total stress is composed of the fluid pressure and the effective solid stress  $\boldsymbol{\sigma}'$  via

$$\boldsymbol{\sigma} = \boldsymbol{\sigma}' - p_f \mathbf{I}. \quad (2.9)$$

Following Jop *et al.* (2006), we decompose  $\boldsymbol{\sigma}'$  into its isotropic and deviatoric components,

$$\boldsymbol{\sigma}' = -p_s \mathbf{I} + \boldsymbol{\tau}, \quad (2.10)$$

where  $p_s = -(1/3)\text{tr}(\boldsymbol{\sigma}')$  and  $\text{tr}(\boldsymbol{\tau}) = 0$ . Further, we impose that the fluid flows relative to the granular material according to Darcy's law,

$$(1 - \phi_s^*)(\mathbf{v}_f - \mathbf{v}_s) = -\frac{k}{\eta_f} (\nabla p_f - \rho_f g \mathbf{e}_z), \quad (2.11)$$

where  $k$  is the permeability of the solid phase.

Combining (2.5), (2.9) and (2.10) under the lubrication approximation, we arrive at

$$\frac{\partial}{\partial z}(p_s + p_f) = -\rho g \quad \text{and} \quad \frac{\partial \sigma'_{xz}}{\partial z} = \frac{\partial}{\partial x}(p_s + p_f), \quad (2.12)$$

along with  $\sigma'_{xx} = \sigma'_{zz} = -p_s$ , while from equation (2.11), the fluid pressure is hydrostatic with  $p_f = P_f + \rho_f g(b - z)$ . It then follows that  $p_s = P_s(x, t) + \phi_s^* \Delta \rho g(h - z)$ , where  $\Delta \rho = \rho_s - \rho_f$  and  $P_s$  is the as-yet unspecified solid pressure at the interface  $z = h$ . As such,

$$\sigma'_{xz} = \sigma_{xz} = \sigma_{xz}(z = h) - (h - z) \left( \frac{\partial P}{\partial x} + \phi_s^* \Delta \rho g \frac{\partial h}{\partial x} \right), \quad (2.13)$$

where  $P = P_f + P_s$ . Further, Darcy's law, equation (2.11), reduces in the lubrication limit to

$$(1 - \phi_s^*)(u_f - u_s) = -\frac{k}{\eta_f} \frac{\partial P_f}{\partial x}. \quad (2.14)$$

Note that the interface solid pressure  $P_s$  must vanish when the solid does not bridge the gap ( $h < b$ ), by continuity of the normal stress, and so  $P_s \neq 0$  only in the bridged region where  $h = b$ .

### 2.1.3. Granular friction

We assume that the internal mechanical interactions between grains obey a Coulomb-like friction model

$$|\sigma'_{xz}| = \mu p_s \quad \text{if } |\sigma'_{xz}| \geq \mu_s p_s, \quad (2.15)$$

$$\frac{\partial u_s}{\partial z} = 0 \quad \text{otherwise,} \quad (2.16)$$

where  $\mu$  is a dimensionless, rate-dependent function, discussed further in §2.2, and  $\mu_s$  is a dimensionless friction coefficient. If the magnitude of the shear stress is sufficiently small, equation (2.16) indicates that beads will resist internal rearrangement and the solid phase acts locally as a rigid body. If the shear stress is sufficiently large, the beads have yielded such that  $|\partial_z u_s| > 0$  and the velocity profile of the beads is chosen such that equation (2.15) is satisfied.

Similarly, we assume that the mechanical interactions between the grains the bottom wall also obey a Coulomb-like friction model:

$$\sigma'_{xz}(z=0) \leq \mu_w p_s(z=0), \quad (2.17)$$

such that

$$u_s(z=0) = 0 \quad \text{if } \sigma'_{xz}(z=0) < \mu_w p_s(z=0), \quad (2.18)$$

$$u_s(z=0) > 0 \quad \text{if } \sigma'_{xz}(z=0) = \mu_w p_s(z=0), \quad (2.19)$$

where  $\mu_w$  is the friction coefficient between the beads and the walls, noting that we assume  $u_s \geq 0$ . A challenge in imposing this boundary condition is that it is not known a priori which of (2.18) and (2.19) applies at each  $x$  location. As such, we regularise equations (2.18) and (2.19) via

$$\sigma'_{xz} = \mu_w p_s \tanh\left(\frac{u_s}{\varepsilon \delta}\right), \quad (2.20)$$

where  $\varepsilon \ll 1$  and all the variables are evaluated at  $z=0$ . This gives a continuous expression for  $\sigma'_{xz}(z=0)$  over the entire  $x$ -domain. The inclusion of the  $\tanh(u_s|_{z=0}/\varepsilon\delta)$  term ensures that  $u_s(z=0) \ll 1$  when  $|\sigma'_{xz}(z=0)| \leq \mu_w p_s$  and satisfies equation (2.19) otherwise. If the beads have not bridged the gap between the plates ( $h < b$ ), we impose that the shear stress is continuous with the fluid layer via equation (2.8). If the beads have bridged the gap ( $h = b$ ), we again apply a regularised Coulomb friction

$$\sigma'_{xz} = -\mu_w p_s \tanh\left(\frac{u_s}{\varepsilon \delta}\right), \quad (2.21)$$

where here all the variables are evaluated at  $z=b$  and the minus sign reflects the different direction of the normal vector.

### 2.1.4. Velocity profile

Before giving specific details of the granular rheology, in Figure 2, we present a selection of example velocity profiles that can occur in the transition zone,  $h < b$  and  $P_s = 0$ , which depend on  $\mu_w$  (the friction coefficient with the walls) and  $\mu_s$  (the internal frictional coefficient). For simplicity, we take  $\sigma'_{xz}(z=h) = 0$ . As such, four profiles arise. When  $\mu_w < \mu_s$ , as with the bridged case, beads will not slide over each other  $\partial_z u_s = 0$ . Beads will slide over the bottom plate if  $\sigma'_{xz}(z=h) = \mu_w p_s$  [Figure 2(a)] or be stationary if  $\sigma'_{xz}(z=h) < \mu_w p_s$  [Figure 2(b)]. When  $\mu_w < \mu_s$ , the entire solid layer will yield  $\partial_z u_s > 0$

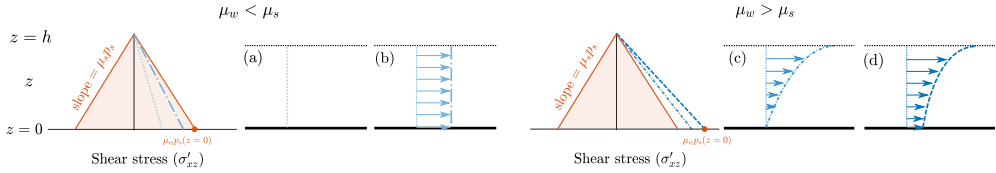


Figure 2: Example illustrations of different velocity-profile configurations for the dry model where  $h < b$ , here assuming  $\sigma'_{xz} = 0$  on  $z = h$  for simplicity. Solid (red) lines denote  $\pm\mu_s p_s$  where  $p_s = \phi_s^* g \Delta\rho (h - z)$ ; these lines give the effective yield stress of the suspension. Dashed and dotted blue lines denote different examples of  $\sigma'_{xz}$  while the red dots denote  $\mu_w p_s (z = 0)$ . Shaded areas denote the region where  $\partial_z u_s = 0$  (the stress is below the yield stress). When  $\mu_w < \mu_s$ , beads will not slide over each other, and may (a) be stationary or (b) slide over the bottom plate. When  $\mu_w > \mu_s$  the entire solid layer must yield with either (c) no slip or (d) slip over the bottom plate.

and beads will either slide over the bottom plate [Figure 2(c)] or be stationary at  $z = 0$  [Figure 2(d)].

Similarly, in Figure 3, we illustrate the different types of velocity profiles that can occur when  $h = b$  (i.e., the grains have bridged the gap). We frame Figure 3 such that  $\mu_w$  increases from (a) to (d) where  $\mu_s$  and  $\sigma'_{xz}$  are fixed. When  $\mu_w < \mu_s$ , Figure 3(a) shows that  $|\sigma'_{xz}| < \mu_s p_s$  across the entire gap such that beads will slide over the plates but not each other, and we arrive at the trivial velocity profile  $u_s = \dot{\delta}$ . When  $\mu_w > \mu_s$ , the beads can still slide over the top and bottom plates, and an internal layer will form where the beads do not yield,  $\partial_z u_s = 0$ , sandwiched between layers where beads do yield,  $|\partial_z u_s| > 0$ , illustrated in Figure 3(b)]. As  $\mu_w$  increases further, the beads will cease to slide over the bottom plate [Figure 3(c)] followed by beads sliding over neither plate [Figure 3(d)]. Over the entire parameter space, we expect the velocity of the beads in contact with the bottom plate to always be smaller than the top plate, because the beads on the bottom experience the weight of the beads.

To accommodate the scenarios shown in Figures 2 and 3, we seek a general velocity profile of the form

$$u_s = \begin{cases} u_{s1}(x, z, t), & \text{if } z \leq h_{y1} \\ u_{s2}(x, t), & \text{if } h_{y1} < z \leq h_{y2} \\ u_{s3}(x, z, t), & \text{if } h_{y2} < z \leq h \end{cases}, \quad (2.22)$$

where  $u_{s1} = u_{s2}$  and  $u_{s2} = u_{s3}$  at  $z = h_{y1}$  and  $z = h_{y2}$ , respectively. The locations of  $h_{y1}$  and  $h_{y2}$  are found by solving  $\sigma'_{xz} = \pm\mu_s p_s$  for  $z$  to give

$$h_{y1} = h - \frac{\sigma'_{xz}(z=h) - \mu_s P_s}{\partial_x P + \phi_s^* \Delta\rho g (\partial_x h + \mu_s)} \quad \text{and} \quad h_{y2} = h - \frac{\sigma'_{xz}(z=h) + \mu_s P_s}{\partial_x P + \phi_s^* \Delta\rho g (\partial_x h - \mu_s)}, \quad (2.23)$$

such that  $\partial_z u_s = 0$  if  $h_{y1} < z < h_{y2}$  and  $|\partial_z u_s| > 0$  otherwise, where  $h_{y1}$  and  $h_{y1}$  represent the locations of the internal yield layers. In the yielded regions ( $0 < z < h_{y1}$  and  $h_{y2} < z < h$ ), we obtain differential equations for  $u_{s1}$  and  $u_{s3}$  by equating equations (2.13) and (2.15).

## 2.2. Granular Rheology

In the region where the grains have yielded,  $|\sigma'_{xz}| > \mu_s p_s$ , we impose a granular rheology that relates the effective viscosity of the solid phase to the inertial number,  $I$ , or the viscous number,  $I_v$ . The specific form of  $\mu$  depends on the magnitude of the Stokes number,  $St = \rho_s d^2 |\partial_z u_s| / \eta_f$ . If the Stokes number is small, viscous forces dominate at the particle scale, while for large  $St$ , inertial forces are dominant. As such, different rheologies are imposed

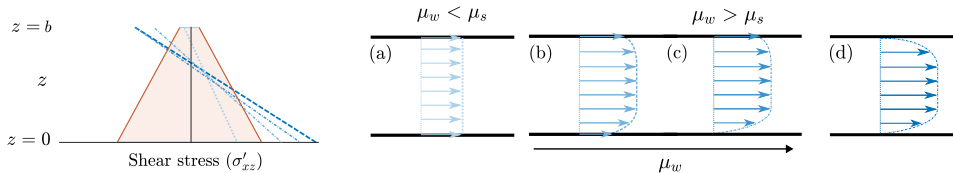


Figure 3: Example illustrations of the different velocity profile configurations when the solid has bridged the gaps between the plates ( $h = b$ ). Solid (red) lines denote  $\mu_s p_s$  and  $-\mu_s p_s$ , where  $p_s = P_s(x, t) + \phi_s^* \Delta \rho g (b - z)$ , with  $P_s > 0$ . Dashed and dotted lines denote different examples of  $\sigma'_{xz}$ . Shaded areas denote the region where  $\partial_z u_s = 0$ . (a) When  $\mu_w < \mu_s$ ,  $|\sigma'_{xz}| < \mu_s p_s$  such that no beads will yield and beads will slide at the same speed as the piston. When  $\mu_w > \mu_s$ , there will be a region where  $\partial_z u_s = 0$  sandwiched between regions where  $|\partial_z u_s| > 0$ . In this case, beads will (b) slide over both top and bottom plates, (c) slide over the top plate but not the bottom, or (d) not slide over either plate.

depending on the Stokes number to capture the correct behaviour. In §3, we consider the case where the fluid phase is negligible,  $\eta_f \ll 1$ , such that the Stokes number is large. In this case, we follow Iordanoff & Khonsari (2004) and Da Cruz *et al.* (2005) and take

$$\mu = \mu_s + \frac{\mu_2 - \mu_s}{I + I_0} I, \quad (2.24)$$

where  $I_0$  and  $\mu_2$  are constants and the inertial number is

$$I = \sqrt{\frac{d^2 \rho_s}{p_s} \frac{\partial u_s}{\partial z}}. \quad (2.25)$$

The form of equation (2.24) comes from fitting from experiments and numerical simulations, such that  $\mu \rightarrow \mu_s$  as  $I \rightarrow 0$  and  $\mu \rightarrow \mu_2$  as  $\mu$  increases. In §4, we consider the influence of the ambient fluid on the grains such that the Stokes number is not necessarily large. In this case, we follow Boyer *et al.* (2011) and take the rate-dependent friction in equation (2.15) to be

$$\mu = \mu_s + \frac{\mu_2 - \mu_s}{I_v + I_0} I_v + I_v + \frac{5\phi_s^*}{2} \sqrt{I_v}, \quad (2.26)$$

where

$$I_v = \frac{\eta_f}{p_s} \left| \frac{\partial u_s}{\partial z} \right|. \quad (2.27)$$

Note that the values of  $I_0$ , and  $\mu_2$  in equation (2.26) are not necessarily the same as those in equation (2.24). The last two terms on the right-hand side of equation (2.26) mean that  $\mu$  will increase without boundary as  $I_v$  increases. By substituting equations (2.24) and (2.25) or (2.26) and (2.27) into (2.15), we arrive at a non-linear ordinary differential equation for  $u_s$  with the boundary conditions given by equations (2.20) and (2.21) at  $z = 0$  and  $h$ , respectively.

### 2.3. Non-dimensionalisation and regularisation

To non-dimensionalise our model, we use  $b$ ,  $b/\dot{\delta}$ ,  $\dot{\delta}$ , and  $\phi_s^* \Delta \rho g b$  as characteristic spatial, temporal, velocity, and pressure scales. The key non-dimensional parameters are then

$$\theta = \frac{\eta_f \dot{\delta}}{b^2 \phi_s^* \Delta \rho g}, \quad K = \frac{k}{b^2}, \quad \text{and} \quad \text{Fr} = \frac{\dot{\delta} d}{b \sqrt{b g}}, \quad (2.28)$$

as well as  $\mu_w$ ,  $\mu_s$ ,  $\phi_s^*$ , and the other constants in the  $\mu(I)$  constitutive laws, where  $K$  is the non-dimensional permeability. Noting that  $\eta_f \dot{\delta}/b$  is a characteristic shear stress,  $\theta$  can be interpreted as a modified Shields parameter describing the ratio of shear forces to the weight of the granular bed. The modified Froude number  $Fr$ , on the other hand, represents a ratio of inertial and gravitational forces, scaled by  $d/b$ . As shown below, we find that the Stokes number  $St = \rho_s d^2 \dot{\delta}/b \eta_f$  delineates which of  $\theta$  and  $Fr$  are important: the ‘dry granular’ rheology ( $St \gg 1$ ) depends only on  $Fr$ , while the ‘wet granular’ model ( $St \ll 1$ ) depends on  $\theta$ . From this point on, we retain our original notation but work in non-dimensional quantities.

The evolution equation for the height of the granular pile, equation (2.2), becomes

$$\frac{\partial h}{\partial t} + \frac{\partial}{\partial x}(\bar{u}_s h) = 0 \quad \text{where} \quad \bar{u}_s h = h_{y1} \bar{u}_{s1} + (h_{y2} - h_{y1}) \bar{u}_{s2} + (h - h_{y2}) \bar{u}_{s3}, \quad (2.29)$$

and

$$h_{y1} = h - \frac{\sigma'_{xz}(z=h) - \mu_s P_s}{\partial_x(P+h) + \mu_s}, \quad \text{and} \quad h_{y2} = h - \frac{\sigma'_{xz}(z=h) + \mu_s P_s}{\partial_x(P+h) - \mu_s}, \quad (2.30)$$

recalling that  $P = P_f + P_s$ . To solve for  $\bar{u}_s$ , and thus  $\bar{u}_{s1}$ ,  $\bar{u}_{s2}$ , and  $\bar{u}_{s3}$ , from equations (2.15) and (2.16) we solve

$$\sigma'_{xz}(z=h) - (h-z) \left( \frac{\partial P}{\partial x} + \frac{\partial h}{\partial x} \right) = \mu p_s, \quad 0 \leq z < h_{y1}, \quad (2.31)$$

$$\frac{\partial u_s}{\partial z} = 0, \quad h_{y1} \leq z < h_{y2}, \quad (2.32)$$

$$\sigma'_{xz}(z=h) - (h-z) \left( \frac{\partial P}{\partial x} + \frac{\partial h}{\partial x} \right) = -\mu p_s \quad h_{y2} \leq z < h, \quad (2.33)$$

with the boundary conditions  $u_{s1}(z=h_{y1}) = u_{2s}(z=h_{y1})$  and  $u_{2s}(z=h_{y2}) = u_{3s}(z=h_{y2})$ . As discussed in §2.2, we consider  $\mu = \mu(I)$  for  $St \gg 1$ , equation (2.24), and  $\mu = \mu(I_v)$  for  $St \ll 1$ , equation (2.26), where the inertial and viscous numbers are

$$I = \frac{Fr}{\sqrt{p_s}} \frac{\partial u_s}{\partial z} \quad \text{and} \quad I_v = \frac{\theta}{p_s} \frac{\partial u_s}{\partial z}. \quad (2.34)$$

Substituting equation (2.24) or (2.26) into equations (2.31)-(2.33) gives a non-linear boundary-value problem for  $u_s$  that must be solved over  $z \leq h$ .

To simplify computation of the shear stress between the bridged and un-bridged regions, we introduce an indicator function  $\chi$  that is 0 and 1 where  $h < 1$  and  $h = 1$ , respectively. As such, the shear stress at  $z = 0$  and  $h$ , given by equations (2.20) and (2.8) or (2.21), respectively, become

$$\sigma'_{xz}(z=0) = \mu_w (P_s + h) \tanh \left( \frac{u_s(z=0)}{\varepsilon} \right), \quad (2.35)$$

$$\sigma'_{xz}(z=h) = \chi \mu_w P_s \tanh \left( \frac{u_s(z=h)}{\varepsilon} \right) + (1-\chi) \left( \frac{h-1}{2} \frac{\partial P_f}{\partial x} - \frac{\theta \cdot u_s(z=h)}{1-\tilde{h}} \right). \quad (2.36)$$

To address the singularity that arises when  $h = 1$  in equation (2.36) we effectively cap the shear stress by choosing,  $\tilde{h} = \min(h, 1-K)$ , recalling  $K$  is the non-dimensional permeability of the beads. For computational purposes, it is easier to consider  $\chi$  as a smooth function of the form

$$\chi = h^n, \quad (2.37)$$

where  $n \gg 1$ . Further, evaluating equation (2.13) at  $z = 0$  gives

$$\sigma'_{xz}(z = h) - \sigma'_{xz}(z = 0) = h \left( \frac{\partial P}{\partial x} + \frac{\partial h}{\partial x} \right), \quad (2.38)$$

$$\frac{dP_s}{dx} = \chi (\sigma'_{xz}(z = h) - \sigma'_{xz}(z = 0)). \quad (2.39)$$

Finally, the incompressibility condition, equation (2.4), becomes

$$1 = h\bar{u}_s - \frac{\bar{k}}{\theta} \frac{\partial P_f}{\partial x} + \frac{1-h}{2} u_s(z = h), \quad (2.40)$$

where  $\bar{k} = Kh + (1-h)^3/12$  is the non-dimensional permeability averaged over the gap between the plates.

We solve the above problem numerically by discretising the domain into equally spaced nodes with  $\Delta x = 5 \times 10^{-3}$ . The spatial derivative in equation (2.39) is approximated by central differencing. By substituting equations (2.35)-(2.40) into (2.31)-(2.33), we have a non-linear system of algebraic equations that are solved to give  $\partial_x P_f$ ,  $P_s$ , and  $u_s$ . By averaging  $u_s$  over the appropriate regions in  $z$ , we compute  $\bar{u}_{s1}$ ,  $\bar{u}_{s2}$ , and  $\bar{u}_{s3}$ , and then solve equation (2.29) for  $h$  by approximating the spatial derivative using a second-order essentially non-oscillatory scheme, and integrate in time using the forward Euler method with  $\Delta t = 10^{-5}$ . For the results below, we fix  $n = 200$ ,  $\varepsilon = 10^{-3}$ ,  $\phi_s^* = 0.6$ .

### 3. Dry model ( $\mu(I)$ rheology, $St \gg 1$ )

We first consider the ‘dry’ limit  $\eta_f \rightarrow 0$  and  $\rho_f \rightarrow 0$ , in which  $St \sim 1/\eta_f \gg 1$ . As discussed in §2.2, we therefore impose the  $\mu(I)$  rheology given by equations (2.24) and (2.34) in the region where  $|\partial_z u_s| > 0$ . Further, as  $\theta \sim \eta_f$ , equation (2.40) indicates for the granular medium,  $\partial_x P_f \sim 0$ . For the following results, we take  $I_0 = 0.3$ ,  $\mu_s = 0.4$ , and  $\mu_2 = 0.7$ , which are typical values for monodisperse glass beads (Jop *et al.* 2006; Pouliquen *et al.* 2006). We then explore the roles of  $\mu_w$ ,  $Fr$ , and  $h_0$ . The parameters  $\theta$  and  $K$  drop out of the model in this limit.

To demonstrate the behaviour of solutions of the model, in Figure 4 we present an example simulation performed with  $Fr = 0.1$  and  $\mu_w = 0.85$ . Our simulation qualitatively reproduces the behaviour illustrated in Figure 1. That is, the grains undergo an initial period where they pile up until the gap between the top and bottom plates is bridged. Once the gap has been bridged, the length of the bridged region grows  $L$ , and the transition region translates at a constant speed. As such, it is convenient to introduce a travelling wave coordinate  $\tilde{x} = x - L$ , such that the bridged region will occupy  $\tilde{x} < 0$  while the transition and undisturbed regions will be where  $\tilde{x} > 0$ . We consider the model to have reached steady state once both the shape and velocity profile of the transition region no longer vary in time.

We compute the velocity profile of the solid phase at steady state over a range of values of  $Fr$  with  $\mu_s < \mu_w < \mu_2$  and  $\mu_w > \mu_2$ , shown in Figure 5, where the red lines are included to denote where the beads are sliding over the walls,  $u_s > 0$  at  $z = 0$  and 1. We recall that  $\mu(I) \rightarrow \mu_2$  as  $I \rightarrow \infty$ , such that  $\mu_2$  gives the saturation point for bead friction as the shear rate becomes large. The case  $\mu_w < \mu_s$  is not considered as beads slide over the walls more easily than other beads in this limit, resulting in the trivial velocity profile  $u_s = 1$  for all  $Fr$  (Figures 2(a) and 3(a)). We investigate the behaviour of the beads in detail in the bridged and transition regions in the following two sections.

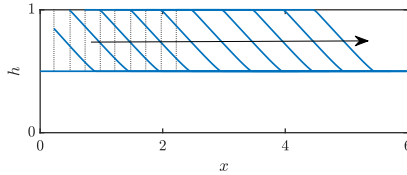


Figure 4: The height of the granular pile computed from solutions to equations (2.29)-(2.40) with  $h_0 = 0.5$ ,  $Fr = 0.1$ , and  $\mu_w = 0.85$ . The dotted black vertical lines denote the location of the piston. The black arrow indicates direction of increasing time, with solutions being plotted in time intervals of 0.25 up to  $t = 2.5$ .

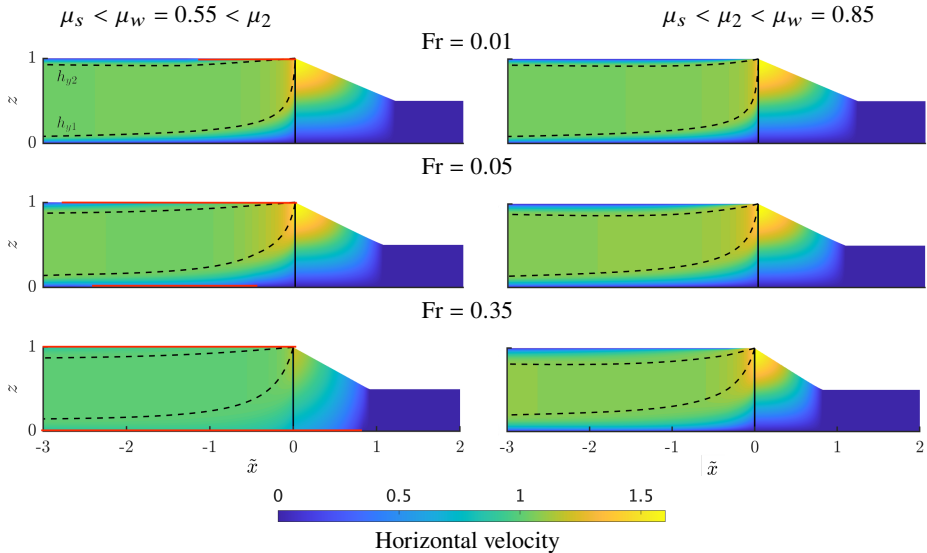


Figure 5: The velocity profile of the solid phase at steady state computed with  $\mu_w = 0.55$  (left) and 0.85 (right). The Froude number (top to bottom) is  $Fr = 0.01, 0.05$ , and 0.35. The dotted black lines denote the location of  $h_{y1}$  and  $h_{y2}$  defined by equations (2.30), recalling that  $\partial_z u_s = 0$  for  $h_{y1} < z < h_{y2}$ . The solid black vertical lines denote the end/start of the bridged/transition regions. The red lines denote the regions where the beads slide over the walls, i.e.,  $u_s > 0$  at  $z = 0$  and 1.

### 3.1. Bridged region

Since  $h$  is prescribed in the bridged region, we do not need to solve equation (2.29) and equation (2.40) simplifies to  $\bar{u}_s = 1$ . However, as discussed in §2.1.2, the velocity profile of the solid phase is not trivial due to the friction experienced by the beads both with the top and bottom plates and each other. As illustrated in Figure 5 row 1, when  $Fr$  is sufficiently small, the beads will yield over the entire gap around the start of the bridged region ( $h_{y1} = h_{y2} = 1$ ), and the beads do not slide over the bottom plate. As the length of the bridged region grows, the beads stop sliding over the top plate, resulting in the velocity profile illustrated in Figure 3(d). When  $\mu_w < \mu_2$  (column 1), as  $Fr$  increases, we find that the beads begin to slide over both the top and bottom plates. Further, for large  $Fr$ , the beads appear to resist internal rearrangement such that  $|\partial_z u_s| \ll 1$  across the entire gap. In comparison, when  $\mu_w > \mu_2$  (column 2), we find that the beads do not slide over the bottom or top plate for all  $Fr$ , and the velocity profile does not appear to change significantly as  $Fr$  is varied.

To better understand the influence of the Froude number and the wall friction parameter, we compute the velocity profile of the beads at  $z = 1$  and 0 over a range of values of  $Fr$  with

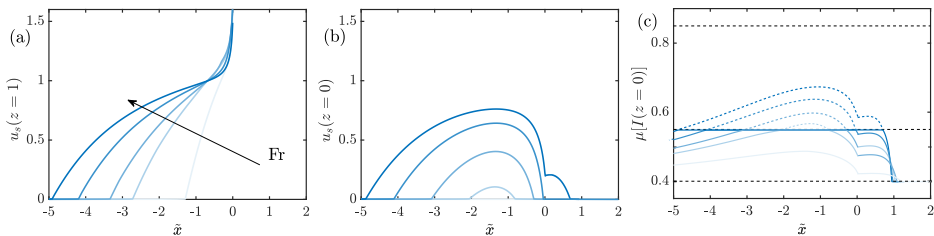


Figure 6: Velocity of the beads on the (a) top and (b) bottom plates with  $\mu_w = 0.55$  and (light to dark blue)  $Fr = 0.01, 0.04, 0.06, 0.1, \text{ and } 0.15$ . Plot (c) shows the friction factor  $\mu(I)$  evaluated at  $z = 0$  for  $\mu_w = 0.55$  (solid) and  $0.85$  (dashed). The dotted black lines denote  $\mu_s = 0.4$ , and the two values of  $\mu_w$  being considered.

$\mu_s < \mu_w = 0.55 < \mu_2$ , shown in Figures 6(a) and (b). The velocity of the beads in contact with the top plate [Fig 6(a)] is fastest at the start of the bridged region and monotonically decreases to 0 as the length of the bridged region grows, after which the beads are stationary. Further, the length of the region where beads slide over the top plate increases with  $Fr$ . For the beads in contact with the bottom plate [Fig 6(b)],  $Fr$  must be sufficiently large or the beads will be stationary over the entire bridged region. When  $Fr$  becomes sufficiently large the beads will begin to slide, which corresponds to the point where  $\mu(I) = \mu_w$  shown in Figure 6(c). However, unlike beads in contact with the top plate, beads will be stationary at the start of the bridged zone, resulting in a region where beads slide sandwiched between regions where the beads are stationary. As  $Fr$  increases further, this region where  $u_s(z = 0) > 0$  will ‘spread’ and the beads at the start of the bridged zone will begin to move (red curves). In comparison, when  $\mu_w = 0.85$ , beads do not slide over either plate for all  $Fr$ . Figure 6(c) indicates that while  $\mu(I)$  (denoted by dashed lines for  $\mu_w = 0.85$ ) increases with  $Fr$  as it does for  $\mu_w = 0.55$ , it will always be smaller than  $\mu_w$ , in this case, because it is bounded above by  $\mu_2 = 0.7 < \mu_w$ .

As the length of the bridged region grows and  $P_s$  becomes sufficiently large, for all  $Fr$  and  $\mu_w > \mu_s$ , the beads will not be able to slide over both the top and bottom plates. Further, as indicated by Figure 7(a),  $h_{y1}$  and  $h_{y2}$  will tend toward 0 and 1, respectively. As such, the velocity profile of the beads will tend to  $u_s \approx 1$ , except for the increasingly thin regions around  $z = 0$  and 1. Such a profile is not observed in experiments, discussed further in section 5, and we anticipate that our continuum approximation will break down when  $h_{y1}$  and  $1 - h_{y2}$  become sufficiently small. When the velocity of the beads in contact with the walls are of order  $\varepsilon$ , Figure 7(b) shows that  $\tanh(u_s/\varepsilon)$  at  $z = 0$  and 1 will tend to  $\mu_s/\mu_w$ , which still satisfies  $u_s \ll 1$ . Thus from equation (2.39), it follows that  $\partial_x P_s \sim -2\mu_s P_s$ , indicating that pressure builds up exponentially through the bridged region, as illustrated in Figure 7(c). By comparison, when  $\mu_w < \mu_s$  where we have the trivial velocity profile  $u_s = 1$ ,  $\tanh(u_s/\varepsilon) \sim 1$  and  $\partial_x P_s \sim -2\mu_w P_s$  resulting in the same exponential behaviour, but not controlled by the wall friction factor. This exponential relationship between the length of the bridged region and the normal stress at the piston is consistent with previous DEM simulations (Marks *et al.* 2015).

### 3.2. Transition zone

We now turn our attention to the behaviour of the transition zone, which, as illustrated in Figure 1(c), is the wedged-shape region with  $h < 1$  and  $P_s = 0$ . In this region, given that the impact of the fluid on the grains is negligible, it follows that  $\sigma_{xz}(z = h) \sim 0$ , and the

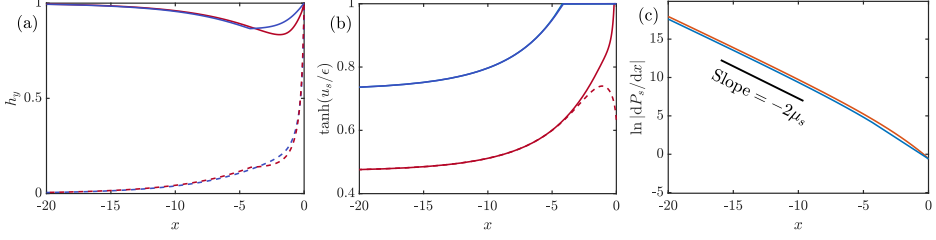


Figure 7: (a) The location of the yield layers  $h_{y1}$  (dashed curve) and  $h_{y2}$  (solid curve) determined by equations (2.30). (b) The hyperbolic tangent of the solid velocity at  $z = 1$  (solid curve) and  $z = 0$  (dashed line), which are used to compute the regularised shear stress according to equations (2.35) and (2.36), recalling that  $\varepsilon = 10^{-3}$ . (c) Natural log of  $|\partial_x P_s|$  computed from equation (2.39). Solutions are computed with  $\text{Fr} = 0.1$  and  $\mu_w = 0.55$  (blue) and  $0.85$  (red).

(non-dimensional) shear stress, equation (2.13), reduces to

$$\sigma'_{xz} = (z - h) \frac{\partial h}{\partial x}. \quad (3.1)$$

As illustrated in Fig. 2, when  $\sigma_{xz}(z = h) = 0$  the entire solid layer will be plugged ( $h_{y1} = 0$  and  $h_{y2} = h$ ) if  $\mu_w < \mu_s$ . If  $\mu_w > \mu_s$ , the solid layer will yield ( $h_{y1} = h_{y2} = h$ ) if  $|\partial_x h| > \mu_s$  or be plugged otherwise. As such, we can reduce equation (2.22) to

$$u_s = \begin{cases} u_s(z = 0) & \text{if } 0 \leq z < h_y \\ u_{sy}(x, z, t) & \text{if } h_y \leq z \leq h \end{cases}, \quad (3.2)$$

where

$$h_y = \begin{cases} 0 & \text{if } |\partial_x h| > \mu_s \\ h & \text{otherwise} \end{cases}. \quad (3.3)$$

As such, we arrive at the so-called Bagnold profile (Andreotti *et al.* 2013) in the yielded region

$$u_{sy} = u_s(z = 0) + \frac{2I_0}{3\text{Fr}} \frac{\partial_x h + \mu_s}{\partial_x h + \mu_2} \left[ (h - z)^{3/2} - (h - h_y)^{3/2} \right], \quad (3.4)$$

where

$$0 = \frac{\partial h}{\partial x} + \mu_w \tanh\left(\frac{u_s(z = 0)}{\varepsilon}\right). \quad (3.5)$$

Further, by substituting the inertial number,  $I = \text{Fr} \cdot \partial_z u_s / \sqrt{h - z}$ , into equation (2.24), we arrive at

$$I = -\frac{I_0(\partial_x h + \mu_s)}{\partial_x h + \mu_2}, \quad (3.6)$$

which combined with equation (2.24) reduces to  $\mu(I) = -\partial_x h$ .

Recall that representative solutions were shown in Figure 5 with  $\mu_2 < \mu_w$  in column 1 and  $\mu_2 > \mu_w$  in column 2. We find that as  $\text{Fr} \rightarrow 0$  (row 1), the height of the pile tends to a straight line of slope  $-\mu_s$ . Further, the beads on the bottom plate are stationary such that the velocity profile takes the form illustrated in Figure 2(b). When  $\mu_w < \mu_2$  (column 1), as  $\text{Fr}$  increases, the length of the transition zone decreases and the beads begin to slide along the bottom plate. For sufficiently large  $\text{Fr}$  (row 3), the beads appear to resist internal

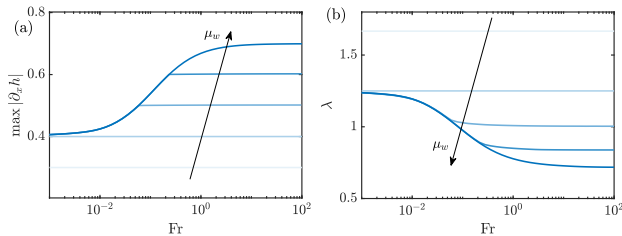


Figure 8: (a) The maximum magnitude of the slope of  $h$ , recalling that  $I = -\partial_x h$ , computed with  $h_0 = 0.5$ ,  $\mu_s = 0.4$ , and  $\mu_w = 0.3, 0.4, \dots, 0.7$ . (b) The corresponding length of the transition region.

rearrangement such that  $|\partial_z u_s| \ll 1$ . When  $\mu_2 < \mu_w$  (column 2), again the slope of the transition zone decreases with increasing  $Fr$ . However, unlike in column 1, the beads remain stationary on the bottom plate for all  $Fr$ . Analogous behaviour was observed in the bridged region discussed previously. For the case where  $\mu_w < \mu_s$  (not shown) the beads do not yield; as such, solutions are independent of  $Fr$  and the height of the pile takes the shape  $\partial_x h = -\mu_w$ .

We compute the maximum magnitude of the slope of  $h$  as a function of  $Fr$  over a range of values of  $\mu_w$  [Figure 8(a)], as well as the corresponding length of the transition zone [Figure 8(b)]. We do this by solving our model for a sufficiently long time such that the shape and velocity of the transition zone are constant. We find that for all  $\mu_w > \mu_s$ ,  $\max |\partial_x h|$ , and in turn  $\max |\mu(I)|$ , will tend to  $\mu_s$  as  $Fr \rightarrow 0$ . This behaviour can be explained by taking  $Fr \rightarrow 0$  with  $u_{s1} \sim \mathcal{O}(1)$  in equation (3.4), which implies that  $\partial_x h \sim -\mu_s$ . When  $\mu_s < \mu_w < \mu_2$ ,  $\max |\partial_x h|$  (and  $\max |\mu(I)|$ ) will monotonically increase with  $Fr$  from  $\mu_s$  and plateau at  $\mu_w$ . Once  $\max |\partial_x h|$  has plateaued, the shear stress is sufficiently large on the base such that the beads will begin sliding,  $u_s(z=0) > 0$ . Given that the inertial number,  $I \sim Fr \cdot \partial_z u_s$ , does not increase above  $\mu_w$  once beads begin sliding along the base, it follows that  $\partial_z u_s \rightarrow 0$  as  $Fr$  becomes large, resulting in the plug-like flow observed in row 3 of Figure 5. Further, taking the limit that  $Fr$  is large, equations (3.4) and (3.5) imply that  $u_s \sim u_s(z=0)$  and  $\partial_x h \sim -\mu_w$ . When  $\mu_w > \mu_2$ , we find that  $\max |\partial_x h|$  will monotonically increase from  $\mu_s$  to  $\mu_2$  with increasing  $Fr$ , while  $\lambda$  will decrease from  $\lambda \rightarrow 1/2\mu_s$  to  $1/2\mu_2$ . As  $\max |\partial_x h| < \mu_w$  for all  $Fr$ , the shear stress at the base is never sufficiently large for the beads to slide over the bottom plate and remain stationary. As such, solutions are independent of  $\mu_w$  for all  $\mu_w > \mu_2$ . In the case where  $\mu_w < \mu_s$ , as discussed above, we find that  $\max |\partial_x h| = \mu_w$  and  $\lambda = 1/2\mu_w$  for all  $Fr$ .

Although  $h$  will tend to a straight line in the limits such that  $Fr$  becomes sufficiently small or large, the shape of the granular pile is not trivial for intermediate values of  $Fr$ . To better understand how the shape of the transition zone varies, we solve for  $h$  over a range of values of  $Fr$  [Figure 9(a)], and extract the corresponding slope [Figure 9(b)]. For small  $Fr$ , the magnitude of the slope of  $h$  tends to  $\mu_s$  as expected. As  $Fr$  increases,  $h$  becomes more non-linear and  $|\partial_x h|$  non-uniformly increases, where the slope is steeper at the start of the transition zone and decreases to 0 by the end. The magnitude of the slope increases with  $Fr$  until it reaches  $\mu_w$ , which corresponds to the point at which the beads will slide along the bottom plate.

We repeat this process for a fixed  $Fr$  across a range of values of  $h_0$  [Figures 10]. For larger values of  $h_0$  (darker blue curves),  $|\partial_x h|$  monotonically decreases over the transition zone. For smaller values of  $h_0$  (blue curves),  $|\partial_x h|$  is non-monotonic such that it initially increases and reaches a peak and then decreases to 0. For sufficiently small  $h_0$ ,  $\max |\partial_x h|$  rises above  $\mu_w$ , suggesting that there will be a region where the beads slide along the base ( $|\sigma'_{xz}| > \mu_w p_s$  at  $z=0$ ) sandwiched between regions where the beads are stationary,  $u_s(z=0) = 0$ .

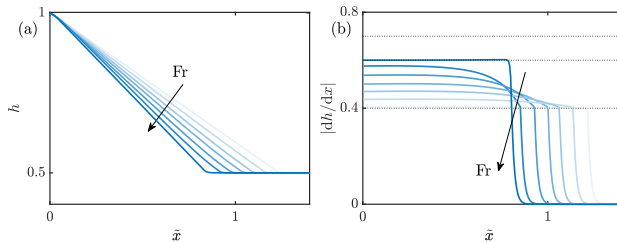


Figure 9: (a) The height of the granular pile for  $h_0 = 0.5$ ,  $\mu_w = 0.6$ , and  $Fr = 0.001$ , 0.017, 0.036, 0.06, 0.1, 0.17, and 1. (b) Corresponding magnitude of the slope of  $h$ . Dotted black lines in (b) denote values of  $\mu_s$ ,  $\mu_w$ , and  $\mu_2$ .

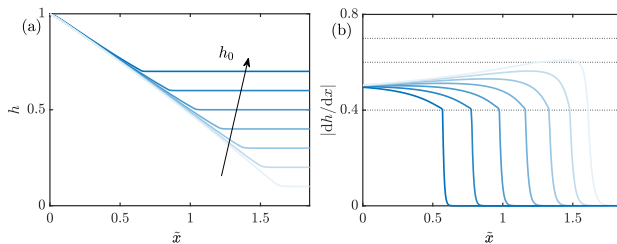


Figure 10: (a) The height of the granular pile for  $Fr = 0.06$ ,  $\mu_s = 0.4$ ,  $\mu_w = 0.6$ , and  $h_0 = 0.1, 0.2, 0.3, 0.4, 0.5, 0.6$ , and  $0.7$ . (b) Corresponding magnitude of the slope of  $h$ . Dashed black lines denote the values of  $\mu_s$ ,  $\mu_w$ , and  $\mu_2$ .

#### 4. Viscous model ( $\mu(I_v)$ rheology)

We turn our attention to the influence of the ambient fluid on the grains. In this case, the Stokes number, recalling  $St \sim 1/\eta_f$ , is not necessarily large, and as such, we impose  $\mu(I_v)$  rheology in the region where the beads have yielded, as discussed in §2.2. For the following results, we take  $I_0 = 0.005$ ,  $\mu_s = 0.32$  and  $\mu_2 = 0.7$  (Boyer *et al.* 2011). Following Figure 5, we compute the steady state velocity profiles over a range of values of  $\theta$ , shown in Figure 11. In the bridged region to the left of the vertical black line, equations (2.40) and (2.11) lead to  $1 = \phi_s^* \bar{u}_s + (1 - \phi_s^*) \bar{u}_f$ , which implies that  $\bar{u}_s = \bar{u}_f$  and  $\partial_x P_f = 0$ . As such, the ambient fluid does not have a direct impact on the behaviour of the beads in the bridged region. While imposing  $\mu(I_v)$  rheology results in a different velocity profile to  $\mu(I)$ , we observe the same general behaviours with both models. That is, we find a non-monotonic profile with a plugged region sandwiched between two regions where the beads slide over one another. However, we find the behaviour of the beads to be noticeably different in the transition region. In particular, Figure 11 shows that the length of the transition region varies non-monotonically with increasing  $\theta$ , initially decreasing (although this is hard to see by eye) before sharply increasing. Furthermore, we are unable to generate steady velocity profiles above a certain value of  $\theta$  because the beads do not bridge the gap between the plates, but rather  $h$  appears to plateau to a value less than 1. We investigate the behaviour of the transition region in detail in the next section.

##### 4.1. Transition zone

To help quantify the influence of the fluid phase on the beads, we introduce the (non-dimensional) horizontal force from the fluid on the grains at the interface between the upper

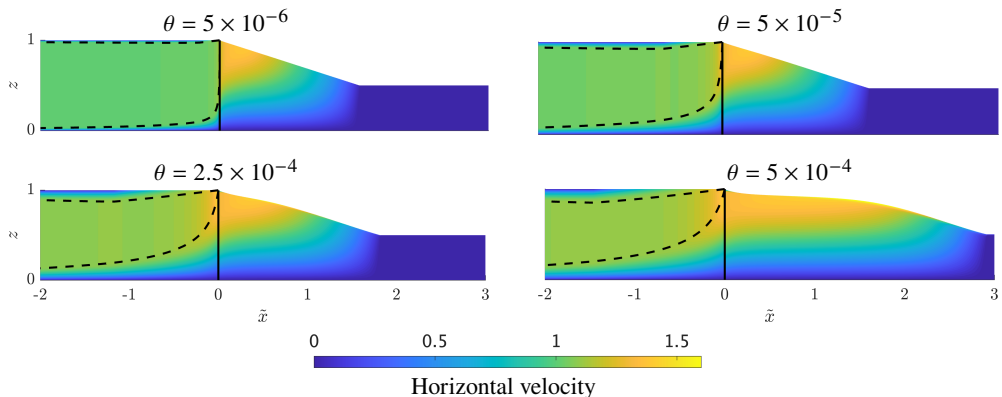


Figure 11: The horizontal velocity profile of the solid phase at steady state computed with  $\mu_w = 0.55$  for different values of  $\theta$ . The dotted black lines denote the location of  $h_{y1}$  and  $h_{y2}$  defined by equations (2.30), recalling that  $\partial_z u_s = 0$  for  $h_{y1} < z < h_{y2}$ .

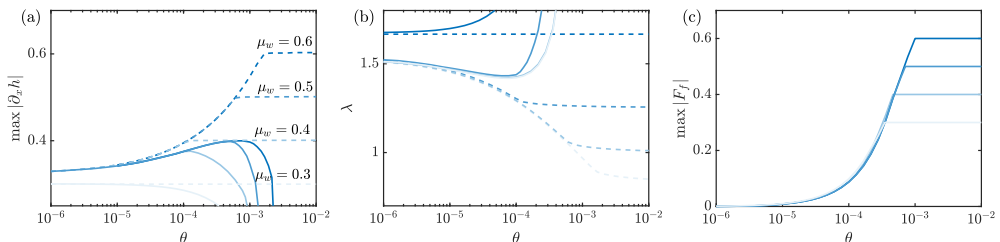


Figure 12: (a) The maximum magnitude of the slope of  $h$ , (b) length of the transition zone, and (c) maximum of the fluid force (4.1). The dashed lines denote the case where the fluid phase is ignored by solving equations (2.29)-(2.40) with  $\partial_x P_f = \sigma'_{xz}(z = h) = 0$ .

and lower layers

$$F_f = \left| \frac{\partial P_f}{\partial x} \right| + \frac{\sigma'_{xz}(z = h)}{h}, \quad (4.1)$$

where  $\max |\mu(I_v)| \approx \max |F_f - \partial_x h|$ . Following on from §3, we compute  $\max |\partial_x h|$  and  $\lambda$  along with  $\max |F_f|$  over a range of values of  $\theta$  and  $\mu_w$ , shown in Figure 12. Additionally, as a point of comparison, we also solve equations (2.29)-(2.40) without the fluid by setting  $\partial_x P_f = \sigma'_{xz}(z = h) = 0$  such that  $F_f = 0$ , denoted by the dashed lines. When  $\theta$  is small (slow pushing), we find that  $F_f \ll 1$  such that the effect of the fluid is negligible. The slope of the pile tends to a straight line with a gradient being the minimum of  $\mu_w$  and  $\mu_s$  [Figure 12(a)], as was observed in the ‘dry’ model in the limit that  $\text{Fr} \rightarrow 0$  discussed in §3. We note that even though imposing either  $\mu(I_v)$  and  $\mu(I)$  will tend to the same limiting shape, each rheology will produce a, at least slightly, different granular velocity profile.

As  $\theta$  increases, Figure 12 indicates that the behaviour of solutions when the fluid is ignored or included will diverge. Specifically, when  $F_f = 0$ ,  $\max |\partial_x h|$  will increase until it plateaus at  $\mu_w$ , at which point the beads will begin to slide on the base as observed with  $\mu(I)$  rheology. However, when the fluid is included in the model, as  $\max |F_f|$  increases, we find that  $\max |\partial_x h|$  and  $\lambda$  are non-monotonic in  $\theta$ , and begin to decrease and increase relative to the  $F_f = 0$  case, respectively. To better understand this behaviour, we consider the shape of the pile of grains for an ‘intermediate’ value of  $\theta$ , shown in Figure 13(a). We find that the length of the transition zone is larger when the fluid is included (solid lines) compared to

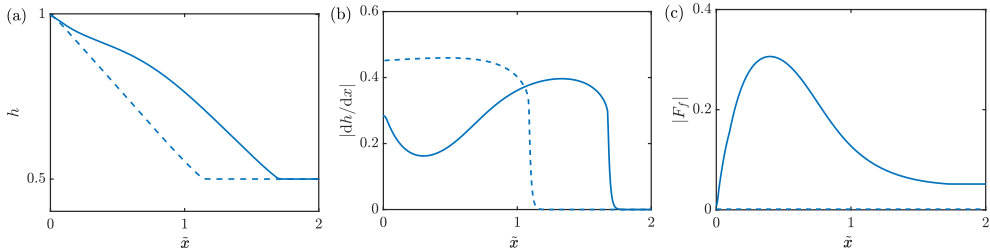


Figure 13: (a) The height of the granular pile computed with  $\theta = 3.6 \times 10^{-4}$  and  $\mu_w = 0.6$ . Plots (b) and (c) are the corresponding magnitude of  $dh/dx$  and fluid force, equation (4.1). The dashed line denotes the case where  $F_f$  is ignored by setting  $\partial_x P = \sigma'_{xz}(z = h) = 0$ . Note that this is distinct from the dry rheology because viscosity is still important for the internal rearrangement of the grains.

when the fluid is ignored (dashed lines). Further, Figure 13(c) indicates there is a peak in fluid force that corresponds to a decrease in  $|dh/dx|$  [Figure 13(b)]. Physically, increasing viscous forces in the fluid phase makes it harder for it to be displaced by the solid as the beads pile up. This effect is exacerbated as  $\theta$  increases, resulting in the sharp increase in the length of the transition zone observed in Figure 12(b).

When  $\theta$  becomes sufficiently large, Figure 12(c) indicates that the maximum fluid force will plateau at  $\mu_w$ . When no fluid is present, beads will slide over the bottom plate when  $|\partial_x h| > \mu_w$ . When the fluid is included, this condition generalises to  $F_f + |\partial_x h| \geq \mu_w$ . As  $F_f \sim \mu_w$ , it follows that  $\partial_x h = 0$  at some value of  $h < 1$ . Physically, viscous forces are balancing the weight of the grains due to friction, preventing the solid from piling up further (Sandnes *et al.* 2011). An additional feature in the large  $\theta$  parameter space is that we can observe bedload transport. That is, the viscous shear from the fluid is sufficient to mobilise the beads over the entire domain such that there is no longer an un-disturbed zone. By imposing that  $\partial_x h = 0$ , equations (2.30)-(2.40) resembles existing models of bedload transport by laminar shearing flows (Aussillous *et al.* 2013; Ouriemi *et al.* 2009), which focuses on determining the critical Shields number for bedload transport to occur, and the resulting velocity profile when it does. In this work, as we are more focused on ‘modest’ values of  $\theta$ , we leave the topic of bedload transport in a confined geometry as an avenue for future work.

## 5. Comparison with Experiments

We present a number of laboratory experiments conducted in a horizontal square glass tube of internal side length  $b = 3$  mm and a piston consisting of a steel rod with a moulded gasket (Vytalex 60). For each experiment, the tube is initially filled with a fluid before the partial loading of wet soda lime glass beads (Honite Blast Media) with  $\rho_s = 2480$  kg·m<sup>-3</sup> sieved to between  $d = 150 - 200$   $\mu$ m. The granular material was fed via a syringe into the tube, angled at approximately 45 degrees, and allowed to fall due to gravity until the formation of a layer of height  $h_0 = 0.75 \pm 0.15$  mm. The piston was driven into the stationary tube by a syringe pump (Harvard PHD Ultra) at a range of velocities. Two interstitial fluids are used - water and a solution of 70wt% glycerol (Fisher Scientific) in water ( $\rho_f = 1181$  kg·m<sup>-3</sup> and  $\eta_f = 2.25 \times 10^{-2}$  Pa·s). Experiments were captured with a Nikon Z6II camera and 105 mm macro lens. We estimate the permeability of the grains via the Kozeny–Carman formula to be  $k = 4.5 \times 10^{-5}$  mm<sup>2</sup>. Over the experimental parameter spaced considered, we find that the largest Reynolds number is about 1.

We compare the height of the granular pile determined from experiments and simulations

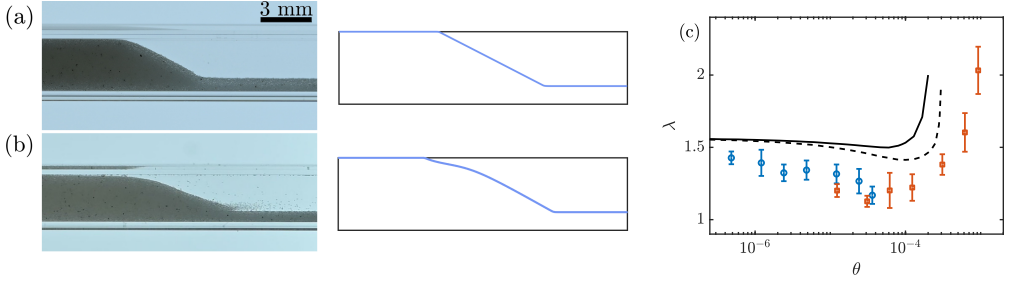


Figure 14: Plots (a) and (b) show snapshots of the experiments and simulations with  $\theta = 4.83 \times 10^{-7}$  (slow pushing, top) and  $1.04 \times 10^{-4}$  (fast pushing, bottom). (c) The non-dimensional length of the transition zone from experiments (symbols) and simulations (lines). Blue and red dots denote experiments performed with water and a solution of 70 wt% glycerol in water, respectively. Solid and dashed black lines denote simulations performed without and with side walls, respectively. Simulations are computed with  $K = 5 \times 10^{-6}$ ,  $\mu_w = 0.53$ ,  $\mu_s = 0.48$ ,  $h_0 = 0.25$ .

in Fig. 14 for a relatively (a) small and (b) large value of  $\theta$ , corresponding to relatively slow and fast piston velocity, respectively. There is broad qualitative agreement between the experiments and simulations. That is, experiments indicate that both the length and shape of the transition region is  $\theta$ -dependent. For low  $\theta$ , the height of the granular pile appears to have a roughly linear profile, while for a larger value of  $\theta$ ,  $\lambda$  and  $h$  appear larger and more non-linear, respectively. In Figure 14(c), we compare the length of the transition zone, which is computed manually from experimental images using the processing software ImageJ, with steady-state measurements of at least three experiments being averaged. Again, both experiments and simulations reproduce the same key behaviours. Specifically,  $\lambda$  is non-monotonic in  $\theta$ , where  $\lambda$  decreases due to the balance of frictional forces between beads and walls, before sharply increasing due to the increasing viscous forces imposed on the grains. We do note however that the experiments predict a lower value of  $\lambda$  compared to the model. One possible reason for this discrepancy is that the influence of the sides of the tube is not included in the model. As such, we extend our model to account for the frictional forces due to the sides of the tube, with details being provided in the Appendix A. We note that the inclusion of side walls in a somewhat ad-hoc fashion, where it is imposed that  $\partial_y u_s = 0$ , may not be a reasonable assumption. Figure 14 shows that the inclusion of side walls (dashed line) into the model improves the agreement with experiments, suggesting they have a significant effect.

We next compare the velocity profiles of the beads from experiments with simulations for a ‘moderate’ value of  $\theta$ , shown in Fig. 15. The velocity profile of the beads is computed from experiments by position-correcting videos to track the start of the transition region and allow for particle image velocimetry (PIV) that was subsequently time-averaged Thielicke & Stamhuis (2014). We find that simulations and experiments are in reasonable agreement with each other. In the transition region,  $\tilde{x} \geq 0$ , experiments show that the velocity profile is monotonically increasing in the vertical direction, and the shear stress at  $z = 0$  is sufficient for the beads to slide over the base, which is consistent with the model. Further, for a smaller  $\theta$  (not shown), beads in contact with the bottom of the tube are stationary, again consistent with simulations. We do note, however, that experiments appear to produce profiles where  $\partial_z^2 u_s > 0$ , while the model produces profiles where  $\partial_z^2 u_s < 0$  for all values of  $\theta$ . Incorporating side walls into the model (dashed lines) can produce profiles where  $\partial_z^2 u_s < 0$ , suggesting again that the presence of the sides of the tube has a significant influence on the dynamics.

Regarding the velocity profile in the bridged region, recall that our model exhibits a piecewise velocity profile of the form of eq. (2.22) illustrated in Figure 3. Figure 15 shows

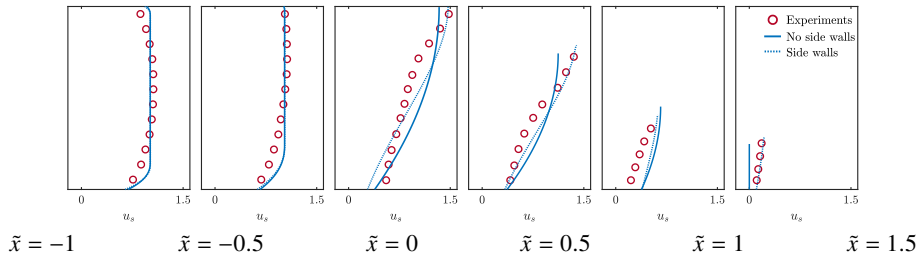


Figure 15: Slices of the non-dimensional velocity profile with  $\theta = 1.23 \times 10^{-5}$  from the model (blue) and experiments (red dots) taken at (left to right)  $\tilde{x} = -1, -0.5, \dots, 1.5$ . The dotted and solid lines denote profiles determined from the model with and without the effects of the side walls, respectively.

that qualitatively, experiments and simulations produce similar behaviour, where beads move slower near the top and bottom walls and faster in the interior, away from the walls. One notable difference between the two is that, unlike the simulations, the experiments do not exhibit a yielded profile in the interior. Unlike in the transition region, accounting for side walls does not appear to have a qualitatively or quantitatively important impact on the velocity profile, and the two scenarios (side walls and no side walls) appear to converge moving to the left, away from the transition region. However, side walls do have an important impact on the bulldozing force. As discussed in §3.1, we find that without side walls  $|\partial_x P_s| \sim 2\mu_w P_s$  in the bridged region; with side walls, the growth rate of the normal stress in the bridged region effectively doubles, such that  $|\partial_x P_s| \sim 4\mu_w P_s$ . We further note that the vertical velocity of the beads (not shown) from experiments is several orders of magnitude smaller than the horizontal component across the entire domain, supporting our assumption of a lubrication-type flow ( $w_s \ll u_s$ ) [§2.1.2].

## 6. Conclusion

In this work, we have presented a continuum model for the bulldozing of a granular material immersed in a fluid-saturated confined geometry. We derived this model by framing the problem as a depth-averaged system of coupled thin films: an incompressible Newtonian fluid overlying a deformable, granular, porous material. To model the frictional forces between adjacent beads, we imposed  $\mu(I_v)$  rheology for the solid phase (or  $\mu(I)$  rheology for the dry case where the fluid is ignored). For beads in contact with the bottom and top plates, we implemented a simple Coulomb friction model such that the shear stress of the solid must be sufficiently large for the beads to slide. By numerically solving our model, we have investigated two specific behaviours - the region where the beads have bridged the gap between the plates (§3.1 and 4) and the behaviour of the beads in the transition zone between the bridged regions and where the beads are stationary (§3.1 and 4.1). In addition, in §5, we provide a comparison of our model with experiments.

In §3, we considered the case where the effect of the fluid on the beads is negligible. When the beads have bridged the gap between the plates,  $h = b$ , we found that the beads exhibit a non-monotonic velocity profile composed of a plugged region  $\partial_z u_s = 0$ , sandwiched between two yielded regions  $|\partial_z u_s| > 0$ . This profile comes from a balance between the rate-dependent frictional stresses the beads experience with each other along with interactions between the beads and the walls of the confining geometry. Further, we find that the normal stress at the piston grows exponentially with the length of the bridged region. In §3.2, we considered the behaviour of the beads in the wedge-shaped region referred to as the transition zone. We found that the shape of the transition zone is dependent on the Froude number,

where generally its length decreases with increasing  $Fr$  due to the beads resisting internal rearrangement as the speed of the piston increases. As with the bridged region, the specific velocity profile and height of the granular pile comes from a balance between how easily beads can slide over the bottom plate in comparison to other beads.

In §4, the effect of the fluid on the grains was considered. We found that for a sufficiently small Shields number  $\theta$ , the influence of the fluid on the grains is negligible and solutions produce the same behaviour as the ‘dry’ model. Specifically, the height of the granular pile tends to a straight line of slope  $\mu_s$  as  $\theta \rightarrow 0$  (that is, the static angle of repose) and steepens towards a slope of  $\mu_w$  (provided that  $\mu_w > \mu_s$ ) as  $\theta$  increases. However, as  $\theta$  becomes large, the effect of the fluid becomes significant and causes the length of the transition zone to increase, which is not observed when the fluid is ignored. This non-monotonic behaviour is consistent with experiments presented in §5, which show a sharp increase  $\lambda$  due to viscous forces imposed by the fluid on the grains. For low  $\theta$ , both the model and experiments predict that the beads in the transition zone will not be able to slide over the bottom plate and the velocity profile will monotonically increase in  $z$ . Similarly for larger  $\theta$ , the shear stress at the base will be sufficiently large such that the beads will overcome frictional forces and slide over the bottom plate. Both the model and experiments produce the same key qualitative behaviours, although it was found that the model is better able to match with experiments when the frictional effects of the side walls of the tube are included, discussed further in §A.

As discussed in §1, one motivation for this work was to provide insight into the behaviour of a granular material bulldozed by a fluid–fluid interface, such as during the injection of a gas into a hydrophilic water-saturated packing. As long as capillary forces are sufficient to prevent the gas from invading the pore space of the packing, this scenario can be thought of as displacing the beads by a deformable piston. Experiments in both capillary tubes (Dumazer *et al.* 2016; Thorens *et al.* 2023) and Hele-Shaw cells (Sandnes *et al.* 2011) show the formation of a variety of patterns resulting from the balance between frictional and capillary forces. With this in mind, an avenue for future work is to extend the two-phase model presented here to incorporate a third phase, a fluid that is non-wetting to the granular packing.

**Declaration of interests.** The authors report no conflict of interest.

## REFERENCES

- ANDREOTTI, B., FORTERRE, Y. & POULIQUEN, O. 2013 *Granular media: between fluid and solid*. Cambridge University Press.
- ARTONI, R. & RICHARD, P. 2015 Effective wall friction in wall-bounded 3D dense granular flows. *Phys. Rev. Lett.* **115**, 158001.
- AUSSILLOUS, P., CHAUCHAT, J., PAILHA, M., MÉDALE, M. & GUAZZELLI, É. 2013 Investigation of the mobile granular layer in bedload transport by laminar shearing flows. *J. Fluid Mech.* **736**, 594–615.
- BAUMGARTEN, A. S. & KAMRIN, K. 2019 A general fluid–sediment mixture model and constitutive theory validated in many flow regimes. *J. Fluid Mech.* **861**, 721–764.
- BOUCHUT, F., FERNÁNDEZ-NIETO, E. D., MANGENEY, . & NARBONA-REINA, G. 2016 A two-phase two-layer model for fluidized granular flows with dilatancy effects. *J. Fluid Mech.* **801**, 166–221.
- BOYER, F., GUAZZELLI, É. & POULIQUEN, O. 2011 Unifying suspension and granular rheology. *Phys. Rev. Lett.* **107**, 188301.
- CASSAR, C., NICOLAS, M. & POULIQUEN, O. 2005 Submarine granular flows down inclined planes. *Phys. Fluids* **17**, 103301.
- DA CRUZ, F., EMAM, S., M., PROCHNOW, ROUX, J. N. & CHEVOIR, F. 2005 Rheophysics of dense granular materials: Discrete simulation of plane shear flows. *Phys. Rev. E* **16**, 021309.
- DOPPLER, D., GONDRET, P., LOISELEUX, T., MEYER, S. & RABAUD, M. 2007 Relaxation dynamics of water-immersed granular avalanches. *J. Fluid Mech.* **577**, 161–181.

- DOROSTKAR, O., GUYER, R. A., JOHNSON, P. A., MARONE, C. & CARMELIET, J. 2017 On the micromechanics of slip events in sheared, fluid-saturated fault gouge. *Geophys. Res. Lett.* **44**, 6101–6108.
- DUMAZER, G., SANDNES, B., AYAZ, M., MÅLØY, K. J. & FLEKKØY, E. G. 2016 Frictional fluid dynamics and plug formation in multiphase millifluidic flow. *Phys. Rev. Lett.* **117**, 028002.
- DUMAZER, G. AND SANDNES, B. AND MÅLØY, K. J. AND FLEKKØY, E. G. 2020 Capillary bulldozing of sedimented granular material confined in a millifluidic tube. *Phys. Rev. Fluids* **5**, 034309.
- ERIKSEN, J. A., SANDNES, B., MARKS, B. & TOUSSAINT, R. 2015a Bubbles breaking the wall: Two-dimensional stress and stability analysis. *Phys. Rev. E* **91**, 052204.
- ERIKSEN, J. A., TOUSSAINT, R., MÅLØY, K. J., FLEKKØY, E. & SANDNES, B. 2015b Numerical approach to frictional fingers. *Phys. Rev. E* **92**, 032203.
- ERIKSEN, J. A., TOUSSAINT, R., MÅLØY, K. J., FLEKKØY, E., GALLAND, O. & SANDNES, B. 2018 Pattern formation of frictional fingers in a gravitational potential. *Phys. Rev. Fluids* **3**, 013801.
- FORTERRE, Y. & POULIQUEN, O. 2008 Flows of dense granular media. *Annu. Rev. Fluid Mech.* **40**, 1–24.
- FREUND, J. B. & ORESCANIN, M. M. 2011 Cellular flow in a small blood vessel. *J. Fluid Mech.* **671**, 466–490.
- FREY, PHILIPPE & CHURCH, MICHAEL 2011 Bedload: a granular phenomenon. *ESPL* **36**, 58–69.
- HAMPTON, M. A., HOMA, J. & LOCAT, J. 1996 Submarine landslides. *Rev. Geophys.* **34**, 33–59.
- HOUSAIS, M., ORTIZ, C. P., DURIAN, D. J. & JEROLMACK, D. J. 2016 Rheology of sediment transported by a laminar flow. *Phys. Rev. E* **94**, 062609.
- IORDANOFF, I. & KHONSARI, M. M. 2004 Granular lubrication: toward an understanding between kinetic and fluid regime. *ASME J. Tribol.* **126**, 137–145.
- IVERSON, R. M. 1997 The physics of debris flows. *Rev. Geophys.* **35**, 245–296.
- JANSSEN, H. A. 1895 Versuche uber getreidedruck in silozellen. *Z. ver. deut. Ing.* **39**, 1045.
- JOP, P., FORTERRE, Y. & POULIQUEN, O. 2005 Crucial role of sidewalls in granular surface flows: consequences for the rheology. *J. Fluid Mech.* **541**, 167–192.
- JOP, P., FORTERRE, Y. & POULIQUEN, O. 2006 A constitutive law for dense granular flows. *Nature* **441**, 727–730.
- KNUDSEN, H. A., SANDNES, B., FLEKKØY, E. G. & MÅLØY, K. J. 2008 Granular labyrinth structures in confined geometries. *Phys. Rev. E* **77**, 021301.
- LANDRY, L. W., GREST, G. S., SILBERT, L. E. & PLIMPTON, S. J. 2003 Confined granular packings: structure, stress, and forces. *Phys. Rev. E* **67**, 041303.
- LEGROS, F. 2002 The mobility of long-runout landslides. *Eng. Geol.* **63**, 301–331.
- MARKS, B., SANDNES, B., DUMAZER, G., ERIKSEN, J. A. & MÅLØY, K. J. 2015 Compaction of granular material inside confined geometries. *Front. Phys.* **3**, 41.
- MAURIN, R., CHAUCHAT, J. & FREY, P. 2016 Dense granular flow rheology in turbulent bedload transport. *J. Fluid Mech.* **804**, 490–512.
- MIDI, G. D. R. 2004 On dense granular flows. *Eur. Phys. J. E* **14**, 341–365.
- MORGAN, M. L., JAMES, D. W., BARRON, A. R. & SANDNES, B. 2020 Self-similar velocity profiles and mass transport of grains carried by fluid through a confined channel. *Phys. Fluids* **32**, 113309.
- OURIEMI, M., AUSSILLOUS, P. & GUAZZELLI, É. 2009 Sediment dynamics. part 1. bed-load transport by laminar shearing flows. *J. Fluid Mech.* **636**, 295–319.
- PAILHA, M. & POULIQUEN, O. 2009 A two-phase flow description of the initiation of underwater granular avalanches. *J. Fluid Mech.* **633**, 115–135.
- PATERSON, L. 1981 Radial fingering in a Hele Shaw cell. *J. Fluid Mech.* **113**, 513–529.
- PENNESTRÌ, E., ROSSI, V., SALVINI, P. & VALENTINI, P. P. 2016 Review and comparison of dry friction force models. *Nonlinear Dyn.* **83**, 1785–1801.
- POULIQUEN, O., CASSAR, C., JOP, P., FORTERRE, Y. & NICOLAS, M. 2006 Flow of dense granular material: towards simple constitutive laws. *JSTAT* **2006**, P07020.
- RETTINGER, C., EIBL, S., RÜDE, U. & VOWINCKEL, B. 2022 Rheology of mobile sediment beds in laminar shear flow: effects of creep and polydispersity. *J. Fluid Mech.* **932**, A1.
- SAFFMAN, P. G. & TAYLOR, G. I. 1958 The penetration of a fluid into a porous medium or Hele-Shaw cell containing a more viscous liquid. *Proc. Math. Phys. Eng. Sci.* **245**, 312–329.
- SANDNES, B., FLEKKØY, E. G., KNUDSEN, H. A., MÅLØY, K. J. & SEE, H. 2011 Patterns and flow in frictional fluid dynamics. *Nat. Commun.* **2**, 288.
- SANDNES, B., KNUDSEN, H. A., MÅLØY, K. J. & FLEKKØY, E. G. 2007 Labyrinth patterns in confined granular-fluid systems. *Phys. Rev. Lett.* **99**, 038001.

- SAURET, A., BALMFORTH, N. J., CAULFIELD, C. P. & McELWAIN, J. N. 2014 Bulldozing of granular material. *J. Fluid Mech.* **748**, 143–174.
- TABERLET, N., RICHARD, P. & DELANNAY, R. 2008 The effect of sidewall friction on dense granular flows. *Comput. Math. Appl.* **55**, 230–234.
- TERZAGHI, K. 1936 The shearing resistance of saturated soils and the angle between the planes of shear. In *First international conference on soil Mechanics, 1936*, , vol. 1, pp. 54–59.
- THIELICKE, W. & STAMHUIS, E. J. 2014 PIVlab – Towards User-friendly, Affordable and Accurate Digital Particle Image Velocimetry in MATLAB. *Journal of Open Research Software* **2**.
- THORENS, LOUISON, MÅLØY, KNUT J, FLEKKØY, EIRIK G, SANDNES, BJØRNAR, BOURGOIN, MICKAËL & SANTUCCI, STÉPHANE 2023 Capillary washboarding during slow drainage of a frictional fluid. *Soft Matter* **19**, 9369–9378.
- ZHANG, DAWANG, CAMPBELL, JAMES M, ERIKSEN, JON A, FLEKKØY, EIRIK G, MÅLØY, KNUT JØRGEN, MACMINN, CHRISTOPHER W & SANDNES, BJØRNAR 2023 Frictional fluid instabilities shaped by viscous forces. *Nat. Commun.* **14**, 3044.

## Appendix A. Influence of side walls

Here we consider the effect of the side walls of the tube, which are located at  $y = \pm W/2$ . We still consider the velocity in the  $y$  and  $z$  directions to be negligible such that  $\mathbf{v}_s = u_s \mathbf{e}_x$ . As such, equation (2.12) becomes

$$\frac{\partial \sigma'_{xy}}{\partial y} + \frac{\partial \sigma'_{xz}}{\partial z} = \frac{\partial}{\partial x}(p_s + p_f) = \frac{\partial P_f}{\partial x} + \frac{\partial P_s}{\partial x} + \phi_s^* \Delta \rho g \frac{\partial h}{\partial x}, \quad (\text{A } 1)$$

recalling  $p_s = P_s + \Delta \rho g \phi_s^*(h - z)$  and  $p_f = P_f + \rho_f g(b - z)$  as before. For simplicity, we assume that the flow is plugged in the  $y$ -direction such that  $u_s \sim u_s(z, t)$  though this is not necessarily true if the aspect ratio of the tube is sufficiently small. By doing so, we average equation (A 1) the  $y$ -direction to get

$$\frac{\partial \sigma'_{xz}}{\partial z} = \frac{\partial P_f}{\partial x} + \frac{\partial P_s}{\partial x} + \phi_s^* \Delta \rho g \frac{\partial h}{\partial x} + \frac{\sigma'_{xy}(y = -b/2) - \sigma'_{xy}(y = b/2)}{W}. \quad (\text{A } 2)$$

Analogous to the friction imposed on the top and bottom plates as described in §2, we have a Coulomb friction condition on the side walls

$$u_s = 0 \quad \text{if } \sigma'_{xz}(z = 0) < \mu_w p_s, \quad (\text{A } 3)$$

$$u_s > 0 \quad \text{if } \sigma'_{xz}(z = 0) = \mu_w p_s, \quad (\text{A } 4)$$

We regularise equations (A 3) and (A 4) analogous to the bottom and top plates via equations (2.20) and (2.21) such that

$$\sigma'_{xy}(y = b/2) - \sigma'_{xy}(y = -b/2) = 2\mu_w (P_s + \phi_s^* \Delta \rho g (h - z)) \tanh\left(\frac{u_s}{\varepsilon}\right). \quad (\text{A } 5)$$

Integrating equation (A 2) with respect to  $z$  gives the expression for the shear stress

$$\sigma'_{xz} = \sigma'_{xz}(z = h) - (h - z) \left( \frac{\partial P_f}{\partial x} + \frac{\partial P_s}{\partial x} + \phi_s^* \Delta \rho g \frac{\partial h}{\partial x} + \frac{2\mu_w (P_s + \phi_s^* \Delta \rho g (h - z))}{W} \tanh\left(\frac{u_s}{\varepsilon}\right) \right). \quad (\text{A } 6)$$

The effect of the side walls can be neglected if  $W$  is sufficiently large. As before, equations (2.15) and (2.16) still apply, where  $\mu(I_v)$  rheology (or  $\mu(I)$ ) is applied in the region where  $|\sigma_{xz}| > \mu_s p_s$  and  $\partial_z u_s = 0$  otherwise.